Modal Blending for Active Flutter Suppression

Jonas Eichelsdörfer *
German Aerospace Center (DLR), 82234 Weßling, Germany

This paper presents a control design methodology for active flutter suppression in parameter-varying aeroservoelastic systems. A rectangular wing exhibiting bending-torsion flutter is modeled in a linear parameter-varying framework. Modal analysis of the critical flutter pole pair shows that both associated eigenvectors are well observed by distributed inertial measurements. Leveraging this property, a least-squares optimal blending of eight accelerometer signals is computed to isolate the flutter dynamics in a two-channel virtual output. A low-order structured H_∞ controller is then synthesized on this reduced interface, targeting robust stabilization up to a specified freestream velocity with prescribed gain and phase margins while minimizing control effort. Relative to an H_2-optimal SISO blending baseline, the proposed approach achieves increased flutter damping and reduced control effort. The architecture further supports sensor fault tolerance by precomputing blending matrices for alternative sensor configurations, enabling reconfiguration without modifying the controller dynamics. Open-source MATLAB code accompanies the paper to facilitate reproducibility and extension to more complex systems.

I. Introduction

Background Flutter denotes a self-excited aeroelastic instability arising from the interaction of unsteady aerodynamics with structural modes, often involving coupling between bending and torsional dynamics [1]. Traditional airframe design mitigates flutter risk by maintaining a large margin to the open-loop flutter boundary, which increases structural weight and constrains the use of high-aspect-ratio, lightweight wings. Active flutter suppression (AFS) aims to increase the damping of critical aeroelastic modes via feedback control, thereby relaxing those structural penalties [2, 3]. The fundamentals of AFS are discussed in [4] and a comprehensive survey is provided by Livne [5].

Related Work Early studies on two-dimensional airfoil sections provided foundational insight into flutter mechanisms and their controllability properties [6, 7]. These works showed that bending-torsion flutter can, in principle, be suppressed through constant feedback of the displacement and/or acceleration in either heave or pitch[8]. A key insight is that effective flutter suppression often hinges on frequency separation between the first bending and torsion modes [9]. While feedback of the heave and/or pitch velocity is an intuitive approach to increase damping, root locus analysis has demonstrated its limited efficacy in cases of closely spaced or coalescing modal frequencies [4]. Furthermore torsion angle feedback tends to outperform bending displacement feedback in terms of achievable damping [10]. The majority of AFS strategies can be broadly divided into collocated SISO feedback and multivariable optimal control. Collocated schemes, in which sensors and actuators share the same location, offer strong robustness properties and design simplicity [11] A prominent example of such collocated control is the *Identically Located Force and Acceleration* concept, which successfully addressed the damping of structural modes of the B-1 aircraft [12–14]. Collocated vertical acceleration feedback enabled the very first AFS flight test in the unstable-region on a B-52 aircraft in 1973 [15]. Further notable publications on collocated feedback for AFS include [16–20]. The more recent research in AFS abandoned the simplicity of a SISO controller. Multivariable optimal control approaches have become prevalent. While H_2-optimal Linear Quadratic Gaussian (LQG) controllers [21, 22] provided a principled starting point, the difficulty of encoding robustness margins limited adoption. Modern AFS is dominated by multivariable H_∞-optimal control [23–28]. Aeroelastic dynamics vary markedly with operating conditions, most notably Mach number and dynamic pressure. Since the aeroelastic states evolve on a much faster timescale than variations in these parameters, the problem is well-suited to a linear parameter-varying (LPV) description, for which a gain-scheduled control offers a natural strategy. [29–32] A complementary line of work pursues *modal isolation*, which aims to decouple specific dynamic modes, e.g. the flutter mode from the residual system dynamics. The method exploits the high-dimensional sensor measurements by forming a linear combination (*blending vector*) of the signals, such that the resulting virtual output isolates the targeted modal state. An analogous procedure may be applied to a multitude of actuator commands, enabling direct excitation of the desired mode. The feedback loop is then closed SISO, substantially reducing overall design complexity. [33–36]

*Research Associate, Institute of Aeroelasticity, jonas.eichelsdoerfer@dlr.de

This Work This paper introduces a systematic modal isolation framework tailored to dominant complex-conjugate eigenvalues (flutter mode). The central idea is to retain *all* independently measurable components of the critical dynamics (generalized position and velocity surrogates), rather than constraining the design to a single blended channel. Concretely this work includes:

1) A least-squares (LS) optimal modal blending framework that (i) constructs output and input blends as (weighted) Moore-Penrose pseudoinverses of the critical output and input pole-vector matrices, (ii) preserves modal quadratures (position/velocity surrogates) and minimum-effort actuation maps exactly on the critical subspace, and (iii) defines a well-conditioned, fault-reconfigurable virtual interface for structured H_∞ synthesis.
2) A Gram-determinant metric for modal controllability and observability that (i) quantifies the independent measurability and excitability of complex-conjugate modes via the squared volume spanned by the corresponding output/input pole vectors, (ii) extends naturally to arbitrary mode subsets, (iii) is insensitive to rotation and common rescaling, and (iv) predicts the conditioning (i.e., noise/effort amplification) of least-squares modal blends.
3) A structured H_∞ controller design (`systune`) on a reduced 2×2 (virtual) interface that balances active structural damping and actuator economy, while maintain robust stability up to a specified freestream velocity with prescribed gain/phase margins.
4) A benchmark comparison against the H_2-optimal SISO blending method of Pusch [36], demonstrating improved flutter damping and reduced control effort in simulation.
5) A practical reconfiguration mechanism for sensor-fault tolerance by precomputing alternative blending matrices for degraded sensor configurations, enabling reconfiguration without changing controller dynamics.
6) An open-source MATLAB implementation for reproducibility and extension.

Paper Organization Section II presents the proposed methodology; Section III introduces the aeroservoelastic benchmark; Section IV details control requirements; Section V summarizes the H_2-optimal blending baseline; Section VI reports design and evaluation results; Conclusions are drawn in Section VIII.

II. Modal Blending Methodology

Modal isolation techniques reduce controller complexity by decoupling critical dynamics from residual modes. However, existing SISO formulations [36] are effectively discarding valuable information if multiple n_c critical poles are to be controlled. This section develops a systematic framework for $n_c \times n_c$ controller structures. The goal is to exploit all relevant information in the measurement signals and, dually, all available actuation capability. At the same time, controller complexity must remain tractable. The modal feedback controller must move all critical poles of a MIMO LTI system into a desired area of the complex plane. Control effort should be minimized and the effect on residual poles must be kept small. For this purpose *static* input/output blends are constructed that (i) concentrate sensing and actuation on the critical modal subspace, while (ii) minimizing spillover onto residual dynamics. Here, *spillover* refers to the unintended excitation or observation of non-targeted modes through the blended channels.

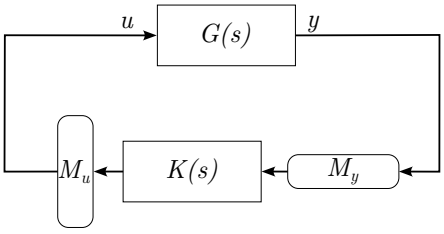

Fig. 1 Block Diagram of proposed Control Method

A. Modal Observability and Controllability

Consider a linear time-invariant (LTI) system of order n with distinct eigenvalues, described by the state-space model

$$\dot{x} = Ax + Bu, \tag{1}$$

$$y = Cx, \tag{2}$$

with n_u control inputs and n_y measurable outputs. The transfer function matrix from inputs to outputs admits the dyadic expansion

$$G(s) = \sum_{i=1}^{n} \frac{C v_i w_i^H B}{s - \lambda_i}, \tag{3}$$

where v_i and w_i^H denote the bi-orthonormal right and left eigenvectors of A ($w_i^H v_j = \delta_{ij}$) associated with distinct eigenvalue λ_i. The factor $w_i^H B$ is referred to as the i-th *input pole vector*, quantifying how strongly mode i is excited by the system inputs. Analogously, the vector Cv_i is the i-th *output pole vector*, indicating how strongly mode i is observed in the outputs [37]. An eigenvalue of an MIMO LTI system is called controllable if its input pole vector is not zero and observable if its output pole vector is not zero, however this existence result provides no degree of "controllability"[37]. Various quantitative measures of modal controllability and observability have been proposed in the literature [38–40]. Of particular relevance in feedback stabilization is the *pole sensitivity* [41], which characterizes the rate at which an eigenvalue can be shifted under constant output feedback.

Pole Sensitivity under Output Feedback For a MIMO system with proportional output feedback $u = -Ky$, the sensitivity of the k-th closed-loop eigenvalue λ_k with respect to the ji-th feedback element k_{ji} is defined as

$$S_{ji}^{\lambda_k} = \frac{\partial \lambda_k}{\partial k_{ji}}. \tag{4}$$

The closed-loop eigenvalue problem reads

$$(A - BKC)v_k = \lambda_k v_k, \tag{5}$$

where v_k is the right eigenvector corresponding to λ_k. Differentiating with respect to k_{ji} gives

$$(A - BKC)\frac{\partial v_k}{\partial k_{ji}} - B\frac{\partial K}{\partial k_{ji}}Cv_k = S_{ji}^{\lambda_k} v_k + \lambda_k \frac{\partial v_k}{\partial k_{ji}}. \tag{6}$$

Multiplying from the left by the associated left eigenvector w_k^H yields

$$w_k^H(A - BKC)\frac{\partial v_k}{\partial k_{ji}} - w_k^H B\frac{\partial K}{\partial k_{ji}}Cv_k = S_{ji}^{\lambda_k} w_k^H v_k + \lambda_k w_k^H \frac{\partial v_k}{\partial k_{ji}}. \tag{7}$$

Using the left-eigenvalue relation

$$w_k^H(A - BKC) = \lambda_k w_k^H, \tag{8}$$

multiplying by $\frac{\partial v_k}{\partial k_{ji}}$, and subtracting the result from Eq. (7), the pole sensitivity becomes

$$S_{ji}^{\lambda_k} = -\frac{w_k^H B \frac{\partial K}{\partial k_{ji}} C v_k}{w_k^H v_k}. \tag{9}$$

For normalized eigenvector pairs ($w_i^H v_j = \delta_{ij}$), this simplifies to

$$\boldsymbol{S}^{\lambda_k} = -(Cv_k)(w_k^H B), \tag{10}$$

that is, the outer product of the k-th mode's input and output pole vectors. Compared to the dyadic expansion of Eq. (3), the sensitivity of eigenvalue λ_k to the feedback element k_{ji} is identical to the negative residue of the transfer function entry $G_{ij}(s)$ at the respective pole $s = \lambda_k$. With suitable scaling of input and output variables, these sensitivities provide meaningful measures of modal controllability and observability [39].

Modal Measures for Real and Complex Poles For a real eigenvalue with normalized eigenvectors, suitable scalar measures of modal controllability and observability are given by

$$|h_i| = \|Cv_i\|, \tag{11}$$

$$|f_i| = \left\|w_i^H B\right\|, \tag{12}$$

where $|h_i|$ represents the effective observability of mode i across all outputs, and $|f_i|$ the effective controllability of mode i via all inputs [39]. For complex eigenvalues, the same procedure applies, but the pole sensitivity becomes complex-valued. For $\lambda_i = \delta + i\omega$,

$$S_{ji}^{\lambda_i} = \Re\left\{S_{ji}^{\lambda_i}\right\} + i\,\Im\left\{S_{ji}^{\lambda_i}\right\}, \tag{13}$$

where $\Re\{S_{ji}^{\lambda_i}\}$ reflects sensitivity of the modal damping $\Re\{\lambda_i\}$, and $\Im\{S_{ji}^{\lambda_i}\}$ reflects sensitivity of the modal frequency $\Im\{\lambda_i\}$.

Proposed Gram-Determinant Measure A measure of independent controllability and observability for complex-conjugate pole pairs (or more generally, for any subset of modes) based on the Gram determinant of the corresponding pole vectors is proposed. Given pole vectors $v_1, v_2, \ldots, v_n$, the Gram matrix is defined as

$$G(v_1, \ldots, v_n) = \begin{pmatrix} \langle v_1, v_1\rangle & \cdots & \langle v_1, v_n\rangle \\ \vdots & \ddots & \vdots \\ \langle v_n, v_1\rangle & \cdots & \langle v_n, v_n\rangle \end{pmatrix}, \tag{14}$$

where $\langle v_i, v_j\rangle = v_i^H v_j$ denotes the Hermitian inner product. The Gram matrix determinant,

$$\Gamma(v_1, \ldots, v_n) = \det G(v_1, \ldots, v_n) \geq 0, \tag{15}$$

quantifies the independence of the respective set of vectors $v_1, v_2, \ldots, v_n$. For a complex-conjugate pole pair $\delta \pm i\omega$ with normalized eigenvectors $v, \overline{v}$ and $w^H, \overline{w}^H$, the proposed observability and controllability measures are

$$\Gamma_H = \det G(Cv,\, C\overline{v})\,, \tag{16}$$

$$\Gamma_F = \det G\left(w^H B,\, \overline{w}^H B\right). \tag{17}$$

Geometrically, the Gram determinant equals the squared volume of the parallelepiped spanned by the given vectors. If any vectors are collinear, the determinant collapses to zero, indicating that the modes cannot be independently measured or controlled. Conversely, values close to one indicate near-orthogonal pole vectors and thus strong independent controllability and observability. Γ is scale dependent with $\Gamma \in [0, 1]$ for sets of unit length (normalized) vectors. In the case of complex conjugate pairs care must be taken. The Gram determinant is equivalent to and may be interpreted in the real two-dimensional subspace spanned by its real embedding $[\Re\{Cv\}, \Im\{Cv\}]$.

B. Least-Squares-Optimal Modal Blending Matrix

Static blending matrices $M_y \in \mathbb{R}^{n_c \times n_y}$ and $M_u \in \mathbb{R}^{n_u \times n_c}$ are proposed that, extract the coordinates of a chosen set of critical modes from the measured outputs and synthesize actuator commands that excite these modes with minimal effort. The *virtual output* and *virtual input* are

$$y_v \;=\; M_y\, y, \qquad u \;=\; M_u\, u_v, \tag{18}$$

and the resulting *virtual plant* G_v retains the essential dynamics of the critical modes while attenuating residual content:

$$G_v(s) \;\triangleq\; M_y\, G(s)\, M_u \;\approx\; \sum_{i=1}^{n_c} \frac{(Cv_i)\,(w_i^H B)}{s - \lambda_i}. \tag{19}$$

The approximation quality and robustness hinge on (a) how independently the critical modes are seen in y and excited by u, and (b) the conditioning of the blends. That is the orthogonality of residual modes input/output pole vectors to the space spanned by the critical pole vectors.

Critical modal subspaces. Let $\{(\lambda_i, v_i, w_i)\}_{i=1}^{n_c}$ denote the eigen-pairs of A for the n_c critical modes to be controlled, with right eigenvectors $v_i \in \mathbb{C}^n$ and left eigenvectors $w_i \in \mathbb{C}^n$ normalized such that $w_i^H v_j = \delta_{ij}$. Define the *critical output* and *critical input* pole-vector matrices

$$C_{\text{crit}} \;=\; \begin{bmatrix} Cv_1 & \cdots & Cv_{n_c} \end{bmatrix} \in \mathbb{C}^{n_y \times n_c}, \qquad B_{\text{crit}} \;=\; \begin{bmatrix} w_1^H B \\ \vdots \\ w_{n_c}^H B \end{bmatrix} \in \mathbb{C}^{n_c \times n_u}. \tag{20}$$

Least-squares modal output blending. Assume C_{crit} has full column rank ($n_y \geq n_c$). The Moore-Penrose pseudoinverse

$$M_y \triangleq C_{\text{crit}}^{\dagger} = (C_{\text{crit}}^H C_{\text{crit}})^{-1} C_{\text{crit}}^H \in \mathbb{C}^{n_c \times n_y} \tag{21}$$

defines the *modal output blending matrix*. For a measured output $y \in \mathbb{R}^{n_y}$, the LS estimate of the critical modal coordinates is

$$\hat{x} = M_y\, y \in \mathbb{C}^{n_c}. \tag{22}$$

This choice of output blending yields the following properties:

- $\hat{y} = C_{\text{crit}} C_{\text{crit}}^{\dagger} y$ is the orthogonal projection of y onto $\text{col}(C_{\text{crit}})$;
- $M_y C_{\text{crit}} = I_{n_c}$, i.e. exact recovery of modal states for $y \in \text{col}(C_{\text{crit}})$;
- $y - \hat{y}$ is orthogonal to $\text{range}(C_{\text{crit}})$, i.e. residual dynamics/noise are rejected in the LS sense;
- $\min_x \|y - Cx\|_2 \longrightarrow \hat{x} = C_{\text{crit}}^{\dagger} y$, is the closest approximation in LS sense.

Least-squares modal input blending. Assume B_{crit} has full row rank ($n_u \geq n_c$). Dually in input space the *modal input blending matrix* is defined as

$$M_u \triangleq B_{\text{crit}}^{\dagger} = B_{\text{crit}}^H (B_{\text{crit}} B_{\text{crit}}^H)^{-1} \in \mathbb{C}^{n_u \times n_c} \tag{23}$$

For a commanded generalized force $f_{\text{mod}} \in \mathbb{C}^{n_c}$, the LS actuation is

$$u_\star = M_u\, f_{\text{mod}} \in \mathbb{R}^{n_u}. \tag{24}$$

This choice of input blending yields the following properties:

- $u_\star = B_{\text{crit}}^{\dagger} B_{\text{crit}} u$ is the projection of u onto $\text{row}(B_{\text{crit}})$;
- $B_{\text{crit}} M_u = I_{n_c}$, i.e. exact realization of commanded generalized forces f_{mod};
- $\min_u \|u\|_2$, subject to $f_{\text{mod}} = B_{\text{crit}} u \longrightarrow u^\star = B_{\text{crit}}^{\dagger} f_{\text{mod}}$;
- $f_{\text{mod}} = B_{\text{crit}} u_\star$, commanded generalized force is achieved with minimum actuator demand.

Complex modes and real coordinates. For complex conjugate pairs $(\lambda, \overline{\lambda})$ with right eigenvectors $(v, \overline{v})$ and left eigenvectors $(w^H, \overline{w}^H)$, real virtual inputs/outputs are obtained by the real-imaginary embedding

$$C_{\text{crit}}^{\mathbb{R}} = \begin{bmatrix} \Re\{Cv\} & \Im\{Cv\} \end{bmatrix}, \qquad B_{\text{crit}}^{\mathbb{R}} = \begin{bmatrix} \Re\{w^H B\} \\ \Im\{w^H B\} \end{bmatrix}, \tag{25}$$

yielding modal coordinates that are linearly equivalent to generalized position and velocity for the corresponding oscillatory mode. The same LS constructions applied to $C_{\text{crit}}^{\mathbb{R}}$ and $B_{\text{crit}}^{\mathbb{R}}$ produce real blending matrices.

Weighted and regularized blending The plain pseudoinverse assumes homogeneous sensor/actuator scaling and white noise.

1) *Output weighting (pre-whitening).* Given a positive-definite weight matrix $W_y \in \mathbb{R}^{n_y \times n_y}$, one may incorporate sensor reliability or noise characteristics. If the measurement noise covariance Σ_y is available, the choice $W_y = \Sigma_y^{-1}$ yields the weighted least-squares projector

$$M_y^{(W)} = (C_{\text{crit}}^H W_y C_{\text{crit}})^{-1} C_{\text{crit}}^H W_y, \tag{26}$$

which maximizes SNR in the chosen metric.

2) *Input weighting.* If one actuator is preferably used choose an actuator penalty $W_u \succ 0$ and use

$$M_u^{(W)} = W_u^{-1} B_{\text{crit}}^H (B_{\text{crit}} W_u^{-1} B_{\text{crit}}^H)^{-1}, \tag{27}$$

which minimizes $u^\top W_u u$ subject to $B_{\text{crit}} u = f_{\text{mod}}$.

Identifiability and the Gram determinant. With Eq. (21) and Eq. (23), the closed-loop design interface is the $n_c \times n_c$ virtual plant

$$G_v(s) \;=\; M_y\, G(s)\, M_u. \tag{28}$$

Decomposing $G = G_{\text{crit}} + G_{\text{res}}$ gives

$$G_v(s) \;=\; M_y\, G_{\text{crit}}(s)\, M_u \;+\; M_y\, G_{\text{res}}(s)\, M_u, \tag{29}$$

where the residual term quantifies spillover. The accuracy and robustness of LS blending depend on (a) the mutual independence of the columns/rows of C_{crit} and B_{crit}, as well as (b) the geometrical and/or frequency separation of the residual poles from the critical poles. For a mode pair, the Gram determinants

$$\Gamma_H = \det\!\big(C_{\text{crit}}^{\top} C_{\text{crit}}\big), \tag{30}$$

$$\Gamma_F = \det\!\big(B_{\text{crit}} B_{\text{crit}}^{\top}\big) \tag{31}$$

coincide (up to normalization) with the observability/controllability measures introduced earlier. Here, the transpose (rather than the Hermitian transpose) is used because the Gram determinants are evaluated on the real embeddings $C_{\text{crit}}^{\mathbb{R}}$ and $B_{\text{crit}}^{\mathbb{R}}$, as defined previously. Values near zero signal poor separability which leads to noise amplification in M_y and excessive actuator demand in M_u. Excessive spillover from residual modes $G_{\text{res}}(s)$ is avoided by separation of the residual modes from the critical modes in frequency ($\Im\{\lambda_r\}$) and/or orthogonality of its input/output pole vector to the space spanned by the critical pole vectors (geometrical separation). If a residual mode is neither separated geometrically nor in frequency, it is advisable to include said mode into the set of critical modes. However, care must be taken to ensure that expanding the set of critical modes does not destroy independent observability/controllability; indicated by $\Gamma_H \approx 0/\Gamma_F \approx 0$. In such case any attempt of independently controlling said critical plant eigen-dynamic is doomed to failure and revisiting plant design - adding sensors, actuator - may be appropriate.

Summary of properties. Under full column/row rank of C_{crit} / B_{crit}, $u_\star = M_u f_{\text{mod}}$ minimizes actuator effort for achieving a desired excitation of the critical modes f_{mod}. And $\hat{x} \;=\; M_y\, y$ yields a LS-optimal approximation of the critical modes states x. These properties make LS blending a natural, interpretable choice for low-order modal controllers (e.g. 2×2 loops on flutter pole pairs).

III. Aeroservoelastic Benchmark Model

To enable the development and evaluation of secondary flight control functions, a representative aeroelastic model of a flexible rectangular wing was constructed and presented in a separate work [42]. The aeroservoelastic benchmark model is methodologically consistent with industry standards yet of comprehensible complexity. The model is linear both in its structural as well as its aerodynamics model. The structural behavior is modeled using a beam-based finite element (FE) formulation capable of capturing bending and torsional deformations, while the unsteady aerodynamic forces are obtained via the Doublet Lattice Method (DLM). The resulting coupled system is transformed into a first-order state-space representation. A Rational Function Approximation (RFA) was used to "translate" the frequency-domain aerodynamics model DLM in the time domain. As a result, a Linear Parameter-Varying (LPV) state-space model is obtained, where the system matrices depend explicitly on the freestream velocity V_∞. This formulation captures the critical dependence of aeroelastic coupling on flight speed and serves as a comprehensible yet physically meaningful benchmark model for the design and testing of active flutter suppression strategies. Figure 2 shows one possible configuration of the benchmark model with a single outboard aileron and 8 distributed vertical acceleration sensors available for secondary flight control.

A. Structural Model

The structural dynamics of a rectangular wing are derived from a beam-based finite element formulation that captures both bending and torsion. The formulation is based on Bernoulli-Euler beam theory for bending, assuming plane sections remain orthogonal to the neutral axis, and Saint-Venant torsion theory, assuming linear torsional displacement. The assembled linear FE model yields second-order structural dynamics of the form:

$$\mathbf{M}_{gg}\ddot{\mathbf{q}}_g + \mathbf{K}_{gg}\mathbf{q}_g = \mathbf{F}_{\text{aero},g} \tag{32}$$

where $\mathbf{q}_g \in \mathbb{R}^{n_g}$ denotes the vector of structural generalized coordinates, i.e. all unconstrained degrees of freedom, and $\mathbf{F}_{\text{aero},g}$ are generalized aerodynamic forces projected onto the structural degrees of freedom.

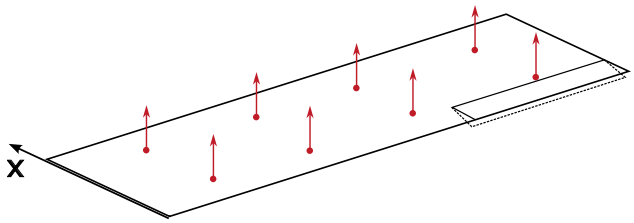

Fig. 2 Wing with distributed IMUs and one Aileron

B. Unsteady Aerodynamics Model

The aerodynamic forces acting on the wing are computed using the Doublet Lattice Method (DLM)[43, 44], which provides a frequency-domain linear potential flow model for oscillating lifting surfaces. The DLM implementation used in this research was provided by Böhnisch and Bangel[45]. The wing is discretized into a rectangular grid of panels along the span and chord, with each panel hosting a doublet at the quarter-chord and a control point at the three-quarter-chord, as shown in Fig. 3. Solving the DLM yields complex-valued aerodynamic influence coefficient

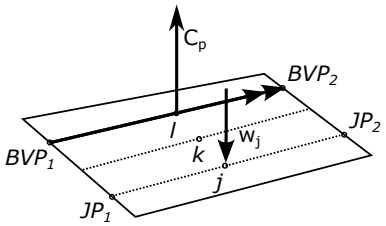

Fig. 3 Unsteady Aerodynamic DLM Panel

(AIC) matrices $\mathbf{Q}_{jj}(k)$, which relate the normalized vertical velocity $w_j(k)$ at control points to the differential pressure coefficients $\Delta c_{p,j}(k)$ on each panel:

$$\Delta c_{p,j}(k) = \mathbf{Q}_{jj}(k) w_j(k) \tag{33}$$

where $k = \omega \frac{c_{\text{ref}}}{2V_\infty}$ is the reduced (dimensionless) frequency. The complex-valued AIC matrix entry Q_{kl} can be thought of as an amplification of the sinusoidal input signal $w_l(t) = \|w_l\| \sin(\omega t)$ by $\|Q_{kl}\|$ and a phase shift by $\angle Q_{kl}$.

To enable time-domain simulation and control synthesis, a Rational Function Approximation (RFA) using Roger's method[15, 46, 47] is applied:

$$\mathbf{Q}_{jj}(s^*) = \mathbf{Q}_{jj}^{(0)} + \mathbf{Q}_{jj}^{(1)} s^* + \sum_{i=1}^{n_p} \frac{\mathbf{Q}_{jj}^{(L,i)} s^*}{s^* + p_i} \tag{34}$$

with $s^* = s \cdot \frac{c_{\text{ref}}}{2V_\infty}$ and lag terms $p_i > 0$. This representation introduces aerodynamic lag states $\mathbf{x}_L \in \mathbb{R}^{n_L}$, governed by:

$$\dot{\mathbf{x}}_L = \mathbf{R}\mathbf{x}_L + \mathbf{E}\dot{w}_j \tag{35}$$

The resulting unsteady aerodynamic forces in generalized coordinates are :

$$\mathbf{F}_{\text{aero},g} = \mathbf{S}_{gj} \left(\mathbf{Q}_{jj}^{(0)} w_j + \frac{c_{\text{ref}}}{2V_\infty} \mathbf{Q}_{jj}^{(1)} \dot{w}_j + \mathbf{D}\mathbf{x}_L \right) \tag{36}$$

C. Aero-Structure-Coupling

Coupling between the structural and aerodynamic sub-models is performed via the principle of virtual work, ensuring energy-consistent interactions. Aerodynamic panel forces are projected onto the structural model using the FEM shape functions evaluated at the aerodynamic panel quarter chord locations, yielding a consistent coupling matrix $\mathbf{S}_{gj}$. Equivalently, structural motion induces aerodynamic downwash velocities at the aerodynamic control points.

$$w_j = \mathbf{D}_{jg}^{\text{Re}} \mathbf{q}_g + \mathbf{D}_{jg}^{\text{Im}} \mathbf{q}_g \tag{37}$$

Combining both structural and aerodynamic states yields the final aeroelastic state vector:

$$\mathbf{x} = \begin{bmatrix} \mathbf{q}_g \\ \dot{\mathbf{q}}_g \\ \mathbf{x}_L \end{bmatrix} \quad . \tag{38}$$

The total number of model states is twice the structural eigenmodes considered plus all lag states introduced by the RFA. In an industry setting, depending on the required model fidelity, the number of states may exceed several hundreds. A significant challenge for controller synthesis[48].

D. Actuator Model

Accurate representation of actuator dynamics is essential for aeroservoelastic controller design, as unmodeled phase loss in the control path can significantly degrade stability margins. Typical control surface deflections servos introduce non-negligible phase lag due to the high frequency nature of flutter suppression. Neglecting this effect typically leads to overly optimistic stability predictions, and compensating for it requires an actuator model that correctly reproduces both the magnitude roll-off and the phase characteristics in the relevant frequency range [49]. In the benchmark model, each control surface is represented by an idealized second-order actuator (PT2 element) with a unit static gain and a prescribed natural frequency and damping ratio. The transfer function has the form

$$G_{\text{act}}(s) = \frac{K\omega_0^2}{s^2 + 2d\omega_0, s + \omega_0^2}, \tag{39}$$

where $K = 1$ ensures unity steady-state gain, $\omega_0 = 32$Hz defines the actuator bandwidth, and $d = 0.9$ sets a moderately damped response. PT2 was chosen in order to provide the current deflection, rate and acceleration of the control surface based on a commanded deflection, whilst keeping the model as simple as possible. The actuator model is supplemented with deflection and rate limits for nonlinear simulation / evaluation. This parameterization yields a realistic phase delay at the comparatively high frequencies of the dominant aeroelastic modes to be controlled, where the actuator phase margin becomes a limiting factor for stabilizing feedback.

E. LPV Model of Benchmark Wing

The wing is equipped with inertial measurement units (IMU) located on the center of the actuator hinge axis. Outputs $\mathbf{y}$ consist of the horizontal (z-axis) acceleration of the wing structure at these points. Control inputs $\mathbf{u}$ are the deflection commands for the trailing edge flaps and leading edge slats. The resulting linear parameter varying state-space model writes

$$\dot{\mathbf{x}} = \mathbf{A}(V_\infty)\mathbf{x} + \mathbf{B}(V_\infty)\mathbf{u} \tag{40}$$

$$\mathbf{y} = \mathbf{C}(V_\infty)\mathbf{x} + \mathbf{D}(V_\infty)\mathbf{u} \tag{41}$$

This LPV formulation captures the essential velocity-dependent coupling between bending and torsion. The resulting flutter dynamics, characterized by the coalescence of bending and torsional modes, are visualized in Fig. 4. Note the aerodynamic panel discretization. This model provides a representative benchmark for developing and evaluating active flutter suppression controllers.

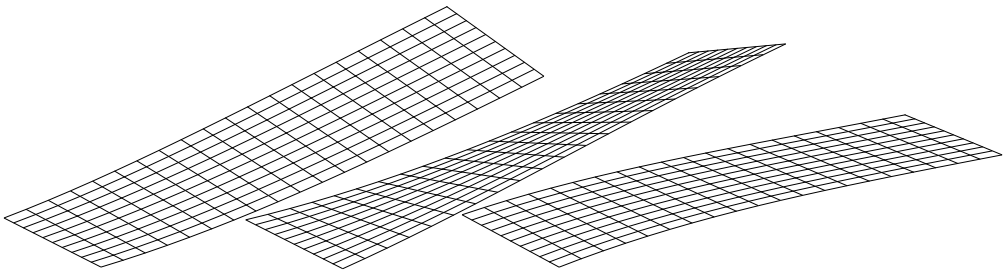

Fig. 4 Flutter Oscillation

The wing dimensions used for this numerical example are taken from the textbook of Wright and Cooper [1]. The open-loop aeroelastic system becomes unstable due to bending-torsion flutter at a freestream velocity of 105 m/s. As can be seen from the pole maps of Fig. 5 bending-torsion flutter is dominated by four critical aeroelastic eigenvalues; i.e. two complex conjugate pairs; i.e. the coalescence of the structural bending and torsion mode. The eigenvalue loci of the benchmark model are depicted at 60 m/s in Fig. 5a and at 120 m/s in Fig. 5b. The stabilizing AFS controller must place

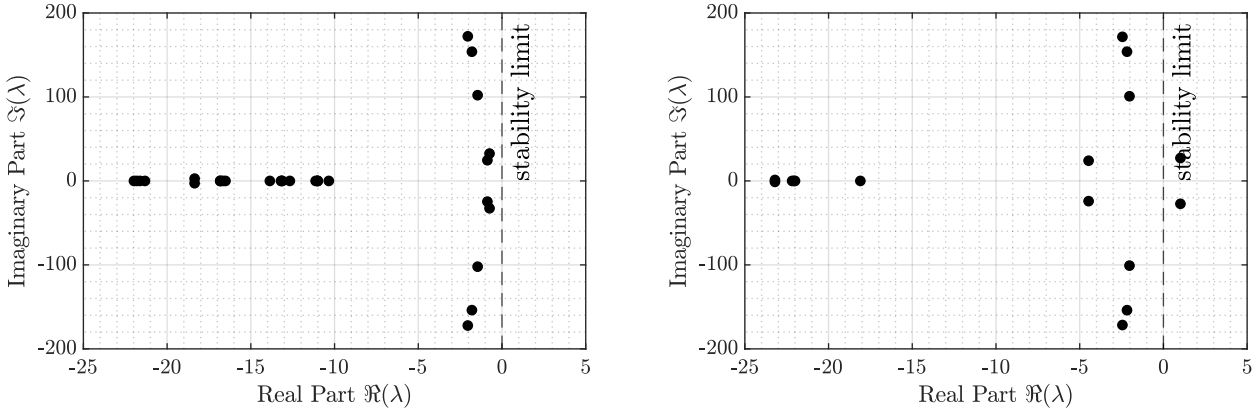

(a) Pole Map at Velocity below Flutter

(b) Pole Map at Velocity in Flutter

Fig. 5 Pole Maps in Stable and Unstable Regime

the open loop unstable pole pair "back" into the left half plane (LHP), whilst minimizing the effect on the residual poles.

IV. Requirements for Active Flutter Suppression

The design of an active flutter suppression (AFS) controller must address fundamental requirements to ensure robust stability, control effectiveness, and fault tolerance. Given the critical nature of AFS systems, these requirements must be met across the full operational envelope while accounting for model uncertainties and potential hardware failures.

A. Robust Stability: Gain and Phase Margins

Active flutter controllers must stabilize an otherwise open-loop unstable system and ensure robust performance across varying flight conditions. Classical robustness metrics such as gain and phase margins provide an accessible means of ensuring controller robustness, with a minimum gain margin of 6 dB and phase margin of 45° often used as baseline targets.[27]

B. Control Activity and Actuator Constraints

The effectiveness of AFS depends largely on the available control authority and bandwidth. The design must ensure that control activity remains within actuator limits (prevent saturation). Key considerations include Bandwidth and Response Time. Actuators must provide sufficient bandwidth to counteract aeroelastic instabilities; Power and Force Limits. Control laws should minimize actuation demand to avoid excessive power consumption and maintenance cost.

In practice actuators, developed for primary flight control, often pose significant constraints on the AFS controller design. Saturation, rate limits, and most notably phase delays must be explicitly accounted for to prevent insufficient active damping or even destabilizing feedback. Control allocation must also reflect actuator effectiveness and redundancy. Livne[5] underscores that modern AFS implementations should consider both "modal participation" and "modal controllability" of each actuator surface. Actuators must be selected and configured to interact constructively with dominant aeroelastic modes, especially under partial failure scenarios. Furthermore, any command strategy must consider energy efficiency and structural fatigue limits. Reducing peak actuator demands not only preserves energy but also enhances system longevity and fault resilience.

C. Fault Tolerance

Given the catastrophic risk associated with loss of flutter suppression, AFS systems must be as fault-tolerant as possible. Fault detection, isolation, and recovery (FDIR) capabilities are essential to mitigate the impact of sensor or actuator failures. The system should employ redundant sensors and actuators, with fault detection algorithms isolating failed components. Control reallocation strategies must redistribute control effort among remaining actuators to maintain stability ("Graceful Degradation"). Redundant sensing technologies must be used to enhance fault resilience.

V. SISO Blending Baseline

As a baseline for active flutter suppression, a modal control strategy based on H_2-optimal blending of inputs and outputs is adopted. This method, originally developed by Pusch and Ossmann[34–36], addresses the challenge of controlling individual modes in over-actuated and over-sensed systems through SISO controllers derived from a high-order MIMO model. The key idea is to construct virtual inputs and outputs via static linear combinations, referred to as blending vectors, which isolate the target mode as effectively as possible.

Given a system's modal decomposition, each oscillatory eigenmode is characterized by a complex conjugate pole pair and associated complex conjugate eigenvectors.

$$\mathbf{G}_i(s) = \mathbf{C}_i \left(s\mathbf{I} - \underbrace{\begin{bmatrix} \Re\{p_i\} & \Im\{p_i\} \\ -\Im\{p_i\} & \Re\{p_i\} \end{bmatrix}}_{\mathbf{A}_i} \right)^{-1} \mathbf{B}_i \tag{42}$$

For a target mode, the H_2-optimal blending approach formulates an optimization problem to jointly maximize the controllability and observability of the mode in terms of the H_2 norm of the resulting SISO transfer function.

$$\max_{\mathbf{k}_y \in \mathbb{R}^{n_y},\, \mathbf{k}_u \in \mathbb{R}^{n_u}} \frac{\left\| \mathbf{k}_y^T \cdot \mathbf{G}_i(s) \cdot \mathbf{k}_u \right\|_{H_2}}{\left\| \mathbf{G}_i(s) \right\|_{H_2}} \quad ; \quad \|\mathbf{k}_y\| = \|\mathbf{k}_u\| = 1 \tag{43}$$

This is achieved by searching for real-valued blending vectors that yield a maximum-energy projection of the input-output transfer through the target mode. The resulting optimization is efficiently solved using a reformulation in terms of the maximum singular value of a phase-rotated residue matrix, allowing a scalar search over the rotation angle. The outcome is a set of input and output blending vectors that define virtual channels for modal control. These channels are then each stabilized using low-order SISO controllers Push demonstrated successful flutter suppression using this synthesis approach[35].

VI. Controller Design

The aeroelastic wing model considered in this research becomes unstable at a freestream velocity of 105 m/s. Prior work has shown that H_∞-optimal robust controllers designed at a single airspeed tend to stabilize the model up to that design point, but not necessarily beyond [50]. In this work a design speed of up to 140 m/s is considered. The classical H_∞ synthesis requires a single linear system to design against. However in this work the simplicity of the convex H_∞ synthesis was traded for the more flexible structured, non-smooth H_∞ synthesis, which allows for optimization against a set of linear models. Hence the linear controller is optimized against the LPV model for freestream velocities ranging from 90 m/s, well below flutter, up to the design speed of 140 m/s. The wing is chosen to incorporate 8 distributed IMUs, measuring vertical acceleration, and one outboard aileron as depicted in Fig. 2. Hence, in the present configuration, modal blending is applied only to the plant outputs (measurements), while the single actuator requires no input blending.

A. Critical Modes and Modal Blending

As can be seen from the pole maps of Fig. 5 bending-torsion flutter is dominated by four critical aeroelastic modes (two complex conjugate pairs). Ideally these four critical aeroelastic eigenvectors are used for blending matrix design, resulting in a $n_c = 4 \times n_y = 8$ output blending matrix M_y. Since only one aileron is considered for flutter suppression in this example there is no input blending necessary. Figure 6 shows the gram determinant of the 2 eigenvectors of the fluttermode as well as the gram determinant of the 4 eigenvectors of the critical aeroelastic modes projected into

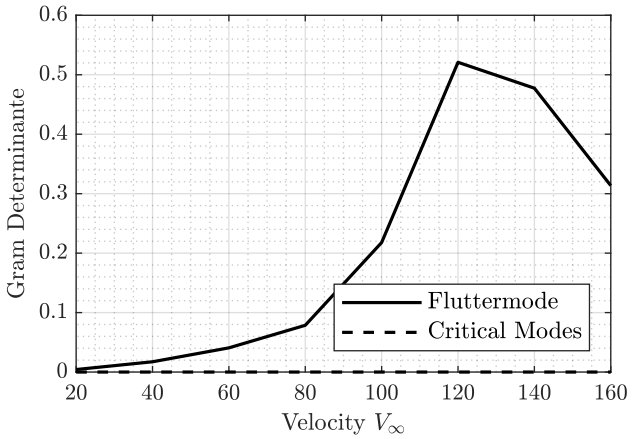

Fig. 6 Gram determinant of flutter & critical modes projection into output space

output space over free-stream velocities V_∞. The independent measurability of the flutter increases sharply around the onset of flutter, then degrades with increasing V_∞ while the four critical aeroelastic eigenvectors are not independently measurable at any V_∞. Since the two dominating complex conjugate pole pairs are not independently measurable solely the fluttermode, i.e. the unstable pole pair, is chosen for modal blending. This choice inevitably leads to spillover from the dropped residual mode, is however the best achievable solution considering the available measurements. The two-dimensional virtual output is constructed using the least-squares optimal projection discussed in ch. II.

$$C^{\mathbb{R}}_{\text{crit}} = \begin{bmatrix} \Re\{Cv\} & \Im\{Cv\} \end{bmatrix}, \tag{44}$$

The $n_c = 2 \times n_y = 8$ modal blending matrix is chosen to optimally separate the two eigenvectors contribution to the measurement output. No additional weighting terms are introduced.

$$M_y = \text{pinv}(C^{\mathbb{R}}_{\text{crit}}) = C^{\dagger}_{crit} \tag{45}$$

This choice isolates the relevant flutter modes generalized position and velocity state in LS sense, acknowledging the trade-off in the form of residual mode spillover. Nevertheless, it ensures tractable and robust synthesis given the measurement limitations.

B. Structured H_∞ Synthesis Problem

Controller synthesis is performed using the structured H_∞ optimization framework implemented in MATLAB's `systune` [51, 52]. This non-smooth optimization method allows minimizing the H_∞ norm of frequency-weighted closed-loop transfer functions while enforcing hard constraints on robust stability margins. Unlike classical H_∞ synthesis, the structured approach permits the designer to prescribe a fixed controller architecture, thereby avoiding the high-order controllers that typically arise from full-order synthesis on aeroelastic plants.

Generalized Plant Formulation. The synthesis is performed on a generalized plant $\mathbf{P}(s)$ that augments the aeroelastic model with disturbance and noise inputs, performance outputs, and the measured acceleration signals. The generalized plant lower fractional feedback interconnection (LFT) is illustrated in Fig. 7. The exogenous input vector w comprises two disturbance channels representing generalized forces on the bending and torsion modes, $d_{q_{f_1}}$ and $d_{q_{f_2}}$, together with sensor noise inputs n_i on each of the eight accelerometers. The performance output vector z includes the generalized modal displacements q_{f_1}, q_{f_2}, their time derivatives $\dot{q}_{f_1}$, $\dot{q}_{f_2}$, and the aileron deflection command δ_{ail}. This formulation enables direct penalization of both structural response and control effort within a single optimization objective.

Static Weight Selection and Physical Interpretation. Following the signal-weighted H_∞ design philosophy [50], the closed-loop specifications are expressed through a combination of static scaling weights and frequency-dependent shaping filters. The static weights normalize the exogenous inputs and performance outputs to unit magnitude, thereby providing direct physical interpretation and facilitating systematic tuning. Four static scaling parameters are employed:

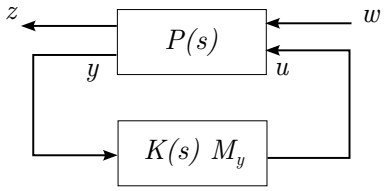

Fig. 7 LFT feedback for structured H_∞ synthesis.

- V_d: the expected maximum magnitude of modal disturbance forces, selected based on the anticipated turbulence intensity and/or gust loads;
- V_n: the expected maximum sensor noise amplitude, determined from accelerometer specifications;
- V_u: the maximum allowable control surface deflection;
- V_p: the performance output scaling, chosen to normalize the modal displacement response to unit magnitude.

For transparency this parameterization separates the frequency-independent amplitude scaling from the frequency-dependent loop shaping. The ratios between these weights directly determine bounds on the closed-loop transfer functions: V_u/V_d bounds the disturbance-to-control transfer function magnitude, V_u/V_n bounds the noise-to-control transfer function, and V_p/V_d bounds the disturbance-to-performance transfer function. For the present design, the weights are selected as $V_d = 0.5$, $V_n = 0.1$, $V_u = 1$, and $V_p = 0.2$, reflecting the relative magnitudes of expected disturbances, sensor noise, available control authority, and acceptable structural response.

Frequency-Domain Weighting and Control Activity Confinement. To shape the closed-loop response in the frequency domain, a second-order bandpass weighting filter $W_u(s)$ is applied to the control effort channel. The filter is constructed as

$$W_u(s) = \frac{(s+\omega_1)(s+\omega_2)}{(s+0.01\,\omega_1)(0.01\,s+\omega_2)}, \tag{46}$$

with corner frequencies $\omega_1 = 12\,\text{rad/s}$ and $\omega_2 = 64\,\text{rad/s}$. This weighting achieves three design objectives that are essential for flutter suppression:

1) *Low-frequency wash-out*: The high-pass characteristic below ω_1 prevents the controller from responding to quasi-static inputs, thereby avoiding interference with rigid-body flight dynamics and autopilot functions that are not modeled in the aeroelastic plant. This wash-out confines control activity to frequencies above the rigid-body bandwidth.
2) *Unity gain in the flutter band*: The approximately unity gain in the frequency range 2–10 Hz (encompassing the flutter modes at 4–5 Hz) permits unattenuated control authority where active damping is most critical.
3) *High-frequency roll-off*: The low-pass characteristic above ω_2 provides robustness against inevitable model uncertainty at high frequencies, suppresses sensor noise amplification, and prevents excitation of unmodeled structural modes.

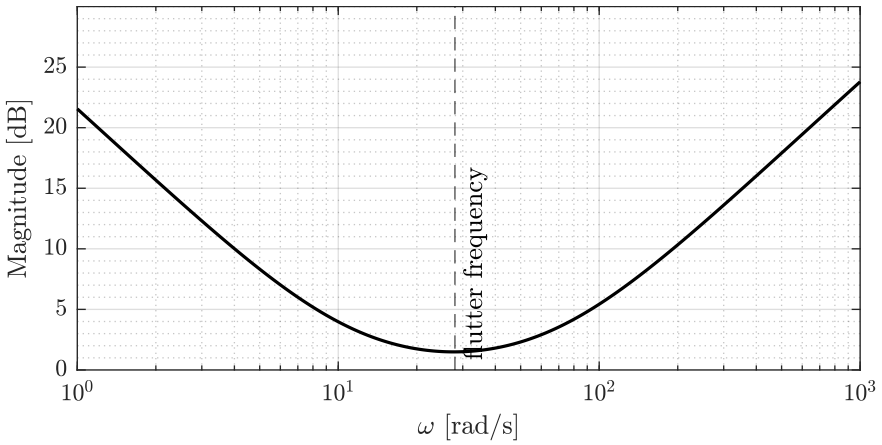

Fig. 8 Weighting Filter for Control Activity

The magnitude response of $W_u(s)$ is depicted in Fig. 8. The inverse weighting $W_u^{-1}(s)$ is used to the control effort performance channels in the generalized plant, such that minimizing the weighted H_∞ norm penalizes control activity predominantly at frequencies outside the flutter band while permitting necessary authority near resonance.

Soft Optimization Objectives and Implied Sensitivity Bounds. Three soft tuning goals are formulated to balance disturbance attenuation against control effort:

1) *Modal displacement attenuation*: The transfer function from disturbance inputs $\{d_{q_{f_1}}, d_{q_{f_2}}\}$ to modal displacements $\{q_{f_1}, q_{f_2}\}$ is constrained by
$$\bar{\sigma}\big(T_{d\to q_f}(i\omega)\big) \;\le\; \frac{V_p}{V_d}, \quad \forall\,\omega. \tag{47}$$
With $V_p = 0.2$ and $V_d = 0.5$, the implied bound of 0.4 directly targets suppression of flutter-induced structural oscillations.
2) *Control effort due to disturbances*: The transfer function from disturbance inputs to actuator command is weighted by $W_u(s)$:
$$\bar{\sigma}\big(T_{d\to \delta_{\text{ail}}}(i\omega)\big) \;\le\; W_u^{-1}(i\omega)\frac{V_u}{V_d}, \quad \forall\,\omega. \tag{48}$$
With $V_u = 1$ and $V_d = 0.5$, this constraint permits a maximum gain of 2 in the flutter band while penalizing actuator activity at frequencies where control is not needed.
3) *Control effort due to sensor noise*: The transfer function from noise inputs to actuator command is similarly weighted:
$$\bar{\sigma}\big(T_{n\to \delta_{\text{ail}}}(i\omega)\big) \;\le\; W_u^{-1}(i\omega)\frac{V_u}{V_n}, \quad \forall\,\omega. \tag{49}$$
With noise scaling $V_n = 0.1$, this objective prevents excessive high-frequency control activity driven by measurement noise, as the implied bound is achieved through the high-frequency roll-off of $W_u^{-1}(s)$.

These soft constraints collectively shape the input sensitivity and control sensitivity transfer functions, indirectly bounding the closed-loop sensitivity function magnitude.

Stability Margins from Bounded Sensitivity. The relationship between the sensitivity function $S(s) = (I + L(s))^{-1}$, where $L(s)$ denotes the loop transfer function, and classical stability margins provides a rigorous foundation for robustness guarantees [37]. If the peak sensitivity is bounded as
$$\|S\|_\infty = \max_\omega \bar{\sigma}\big(S(i\omega)\big) \le M_S, \tag{50}$$
then the closed-loop system is guaranteed to possess minimum gain and phase margins given by
$$\text{GM} \ge \frac{M_S}{M_S - 1}, \qquad \text{PM} \ge 2\arcsin\left(\frac{1}{2M_S}\right). \tag{51}$$
For instance, a peak sensitivity of $M_S = 2$ (equivalently 6 dB) implies a gain margin of at least 2 (6 dB) and a phase margin of at least 29°. This relationship arises from the geometric interpretation of sensitivity: $|S(i\omega)|$ equals the inverse of the distance from the Nyquist curve $L(i\omega)$ to the critical point -1. Bounding $|S(i\omega)| \le M_S$ ensures that the Nyquist curve remains outside a disk of radius $1/M_S$ centered at -1, thereby guaranteeing a minimum distance to the critical point.

Hard Stability Margin Constraint. While the soft objectives implicitly shape the sensitivity function, robust stability is explicitly enforced through a hard constraint on classical loop margins at the plant input (actuator command injection point). The constraint requires a minimum gain margin of 6 dB and a minimum phase margin of 45°:
$$\text{GM} \ge 6\,\text{dB}, \qquad \text{PM} \ge 45^\circ. \tag{52}$$
These margins are evaluated in the *disk margin* sense [53], which provides a combined gain-phase robustness guarantee more stringent than separately specified margins. Unlike classical single-loop margins that consider gain and phase variations independently, disk margins account for simultaneous perturbations and thereby avoid the pitfalls of overlooking destabilizing combinations that individually appear safe. This hard constraint ensures that the synthesized controller maintains adequate robustness against multiplicative uncertainties at the plant input, including unmodeled actuator dynamics and gain variations.

Controller Structure and Modal Blending Integration. The controller is parameterized as a fourth-order linear time-invariant state-space system with a single scalar output (aileron command) and two inputs corresponding to the virtual modal coordinates. The tunable controller $K_{\text{tune}}(s) \in \mathcal{RH}_\infty^{1\times 2}$ is cascaded with the modal output blending matrix $M_y \in \mathbb{R}^{2\times 8}$ derived in Section VI.A:

$$K(s) = K_{\text{tune}}(s) \cdot M_y. \tag{53}$$

This factorization decouples the static sensor fusion (blending) from the dynamic compensation (tunable controller), enabling independent reconfiguration of M_y for fault tolerance without retuning the controller dynamics. The fourth-order structure was determined through iterative refinement; lower orders proved insufficient for achieving the required margin constraints, while higher orders yielded negligible performance improvement.

Multi-Model Optimization. To ensure robust performance across the flight envelope, the synthesis is performed simultaneously against a discrete set of linearized plant models at freestream velocities $V_\infty \in \{90, 100, \ldots, 160\}$ m/s. This range spans from well below the open-loop flutter boundary (105 m/s) to the design speed of 140 m/s and beyond. The `systune` algorithm jointly optimizes the controller parameters to minimize the worst-case soft objective across all models while satisfying the hard margin constraint at every operating point. This multi-model approach obviates the need for explicit gain scheduling while providing point-wise stability and performance guarantees throughout the velocity range.

Optimization Algorithm and Initialization. The non-smooth optimization problem is solved using the algorithm described in [51], which combines bundle methods with specialized handling of non-differentiable H_∞ objectives. To mitigate sensitivity to local minima, the optimization is initialized from eight randomized starting point. Parallel computation accelerates the multi-start search. The best solution across all initializations is retained, with the final controller achieving soft objective values below unity and satisfying all hard constraints (robust stability margins).

VII. Controller Evaluation

This section evaluates the performance and robustness of the structured modal blending controller developed in Section VI.B, with comparisons drawn against the baseline H_2-optimal blending strategy. Emphasis is placed on frequency-domain and time-domain performance metrics as well as actuator demand. All time simulations as well as Sigma plots are evaluated at a freestream velocity of $V_\infty = 130$m/s, well in the unstable flutter region.

A. Robust Stabilization

The modal blending controller achieves robust stabilization across the required range of freestream velocities. Figure 9 compares classical Vg-, $V\omega$-Plots of the Modal and the H_2-optimal blending controllers. Open Loop flutter at $V_\infty = 105$ m/s and 4.5 Hz is indicated by the red circles. An interesting dynamic interaction is observed under the H_2-optimal baseline controller: the two dominant flutter-related modes exhibit a frequency crossing just above the open-loop flutter speed, then diverge at higher velocities. This crossing behavior is absent under the modal blending controller, which maintains clear frequency separation between the modes. Nevertheless, both controllers maintain positive damping across all velocities of interest, with the modal controller providing consistently superior damping on both critical modes throughout the open loop flutter regime. Pole trajectory analysis, see Fig. 10, confirms the stabilization effect. The critical aeroelastic poles, remain firmly in the left half of the complex plane (LHP) under closed-loop conditions for both controllers.

B. Disturbance Rejection and Modal Damping Performance

Modal damping performance is quantified through singular value analysis of the closed-loop transfer function from disturbance forces to structural deformation outputs. Figure 11 shows that the modal blending controller significantly attenuates the peak response to disturbances, in the flutter-critical frequency band around 4.5 Hz. This indicates effective suppression of flutter-induced structural oscillations. In accordance with Bode's sensitivity integral, sensitivity reduction near the resonance frequency necessarily leads to sensitivity amplification elsewhere (the "waterbed effect") [54]. The H_2-optimal controller exhibits slightly improved performance in non-critical bands, but the modal controller outperforms it decisively in the flutter band, precisely where robust damping is most critical. This pronounced reduction in the resonance peak confirms the enhanced damping effect. The residual sensitivity is spread evenly across adjacent

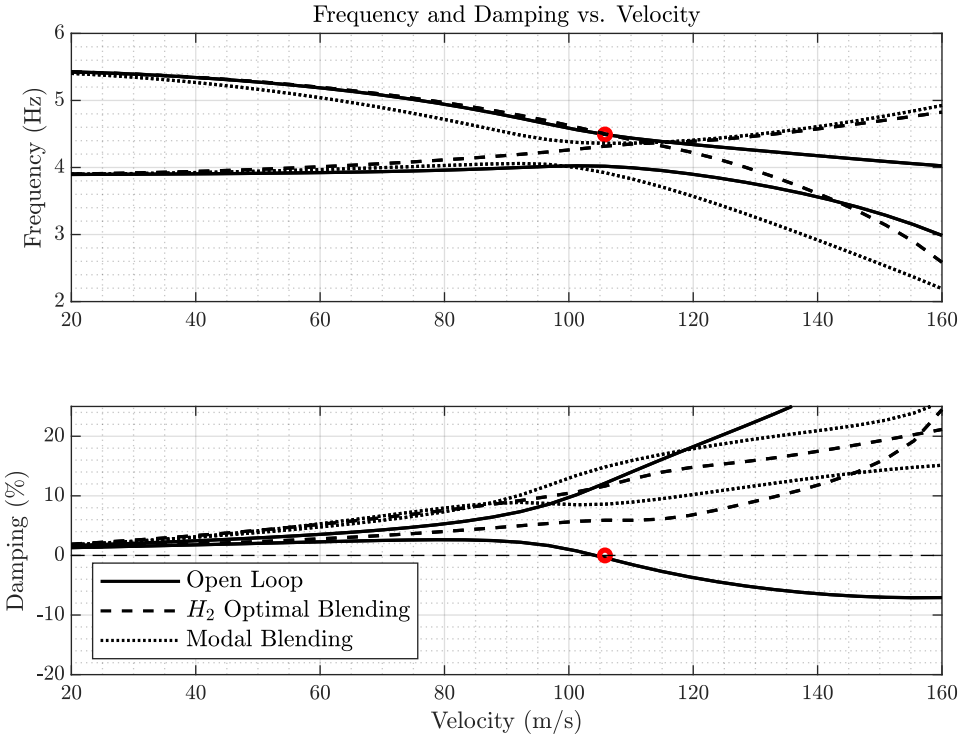

Fig. 9 Vg-Plot and $V\omega$-Plot of Open Loop vs. H_2 Blending vs. Modal Blending

frequency bands, avoiding concentrated amplification and ensuring well-balanced closed-loop behavior. Time-domain validation is provided in Fig. 12 via a frequency sweep excitation applied to the bending mode. The disturbance input sweeps linearly from 0 to 8 Hz over a 16-second interval. The resulting structural response shows excellent damping of mid-frequency content. The modal controller effectively attenuates oscillations near the flutter frequency, outperforming the baseline especially around resonance.

C. Actuator Demand

To assess control effort, actuator deflections are extracted from the same time-domain simulations. Figure 13 shows the corresponding aileron commands. As expected, actuator activity peaks near the flutter frequency. Notably, the modal controller achieves improved damping with less deflection at resonance compared to the H_2-optimal controller. At frequencies away from resonance, however, the baseline controller demands less effort. This phenomenon is further examined in Fig. 14, which plots the singular values of the transfer function from disturbance inputs to actuator commands. The modal controller exhibits a relatively flat response, whereas the H_2-optimal controller achieves less actuator demand outside the flutter band but at the cost of a peak near resonance. This control effort spectrum of the modal controller is a direct consequence of the H_∞ synthesis objective, which minimizes the peak norm rather than integrated energy. One possible explanation for the lower integrated actuator demand of the baseline controller is the restricted control space inherent to SISO design. This restriction may have an effect similar to suboptimal H_∞ synthesis, which is known to yield solutions closer to H_2/LQR-optimal behavior than the true H_∞-optimal solution. Therefore including more sophisticated measures of control effort into the soft optimization objectives may be advantages outside the critical flutter frequency band; But was beyond the scope of this work.

D. Sensor Fault Tolerance

The blending matrix approach is ideally suited for sensor fault tolerance. The blending matrix is linear sensor fusion scheme. In the event of sensor failure, precomputed alternative blending matrices can be employed to reconstruct the modal output using a reduced sensor set, without altering the controller itself. This modular reconfiguration capability

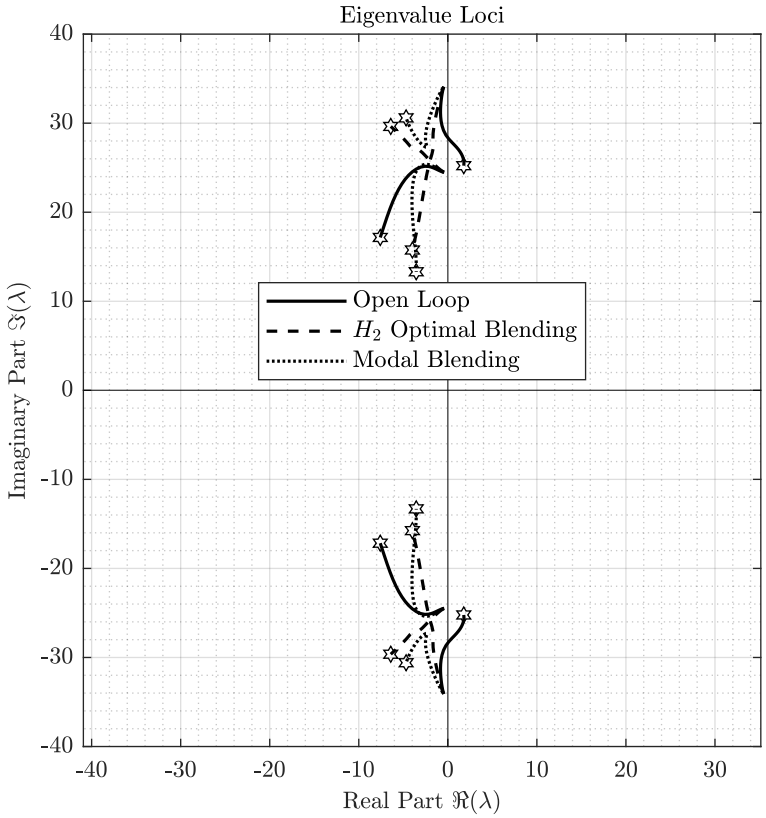

Fig. 10 Pole-Map of Open Loop vs. H_2 Blending vs. Modal Blending

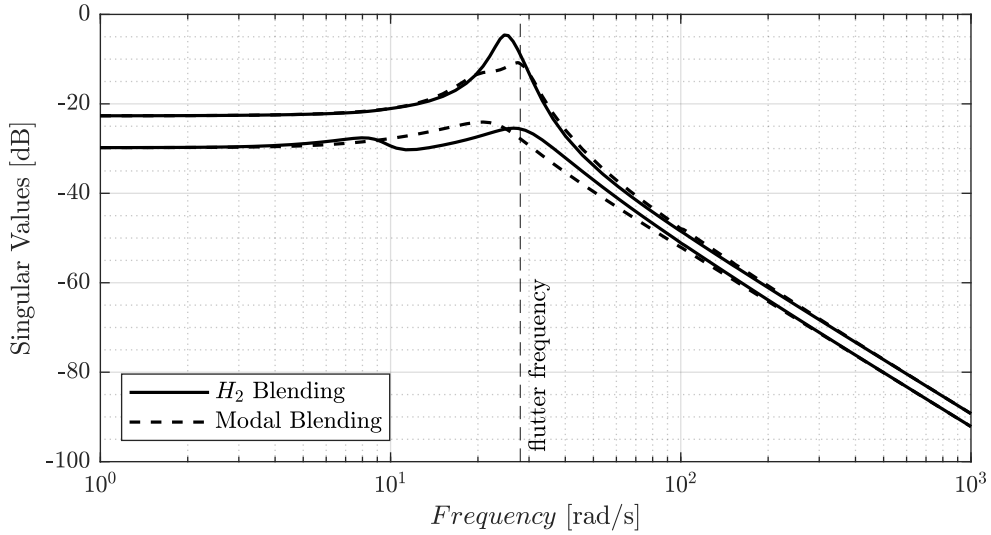

Fig. 11 Singular Values from Disturbance to Structural Deformation H_2 Blending vs. Modal Blending

enhances fault tolerance and supports graceful degradation, assuming sufficient measurement redundancy.

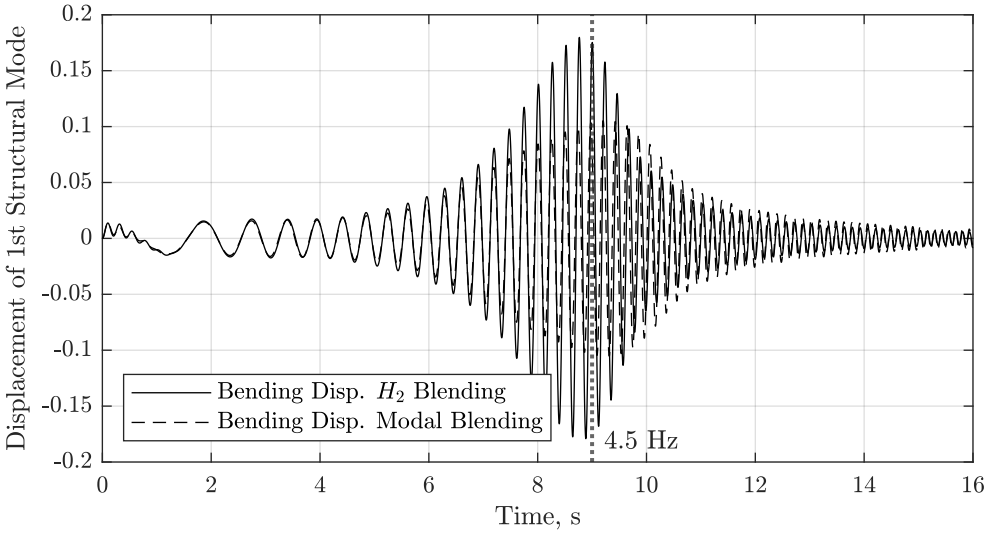

Fig. 12 Time-Simulation Frequency Sweep Disturbance H_2 Blending vs. Modal Blending

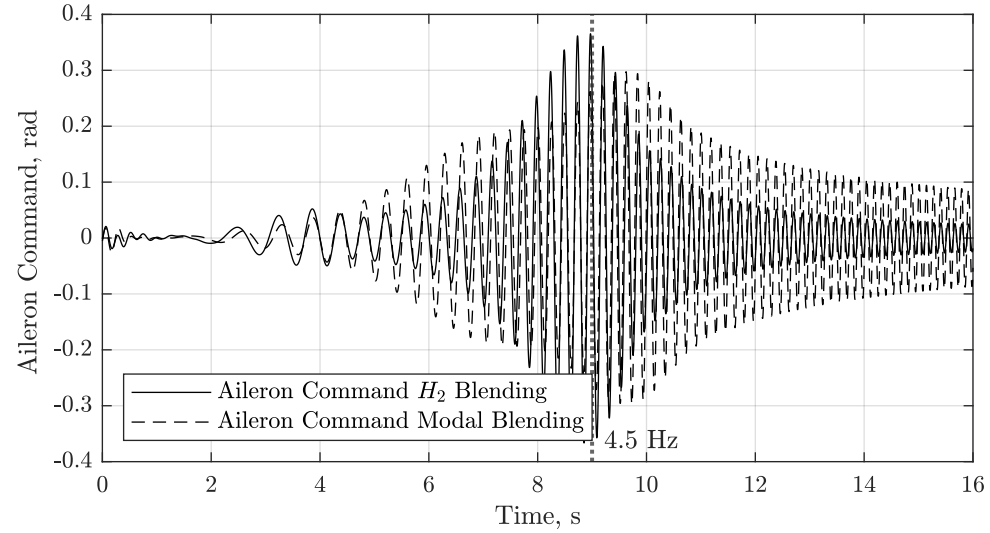

Fig. 13 Time-Simulation Frequency Sweep Disturbance H_2 Blending vs. Modal Blending

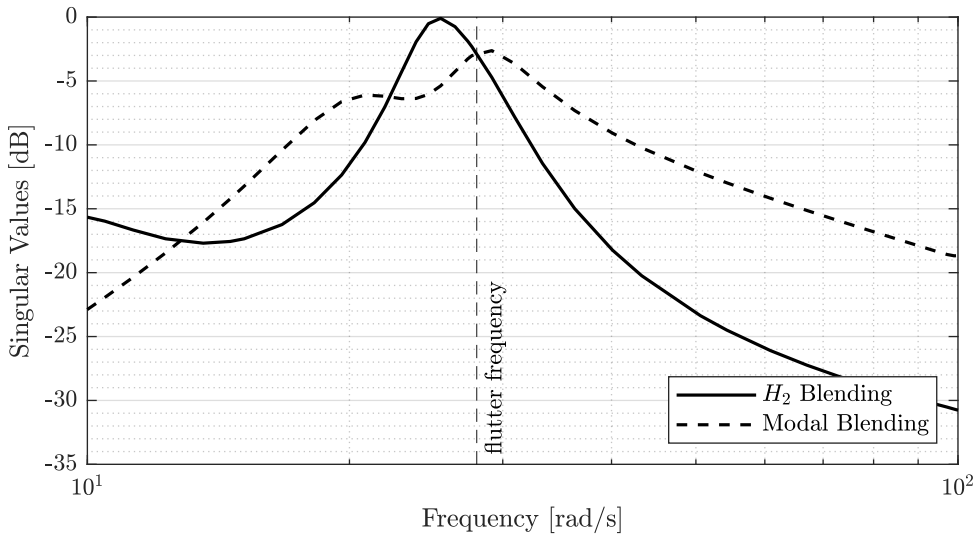

Fig. 14 Singular Values from Disturbance to Actuator Demand H_2 Blending vs. Modal Blending

VIII. Conclusion

This paper introduced a modal control synthesis strategy for active flutter suppression tailored to systems with distributed sensing. Using an aeroservoelastic model of a rectangular wing as a benchmark, the critical flutter mode was isolated via pseudoinverse-based sensor blending, with the blending matrix constructed from the mode's output pole vectors. The resulting two-dimensional output enabled the use of structured H_∞ synthesis to design a robust and efficient minimal controller using only a single control output and two pseudo-measurements. Compared to H_2-optimal blending, the new approach achieved improved damping of the flutter mode and lower actuator demand, particularly at problematic flutter frequency ranges. The method also supports fault-tolerant operation by permitting straightforward reconfiguration of the sensor blending stage.

All results are supported by open-source MATLAB code at github.com/JonasEiche/FlutterWing, enabling reproducibility and extension to more complex configurations such as full aircraft models.

Acknowledgments

The author is thankful to Dr. Gertjan Looye for his encouragement and for the many fruitful discussions that helped shape this work. The author, Jonas Eichelsdörfer, received a scholarship by Munich Aerospace e.V.

References

[1] Wright, J., and Cooper, J., *Introduction to aircraft aeroelasticity and loads*, second edition ed., Aerospace series, Wiley, Chichester, West Sussex, England, 2015. Includes bibliographical references and index.

[2] Thompson, and Kass, "Active Flutter Suppression - An Emerging Technology," *Journal of Aircraft*, Vol. 9, No. 3, 1972, pp. 230–235. https://doi.org/10.2514/3.58962.

[3] Butz, H., Friedrichs, R., Jens and; Henke, and Hornung, M., "The Energy-Efficient Aircraft of the Future – A Long-Term Perspective," Tech. rep., The German Society for Aeronautics and Astronautics, 2025.

[4] Horikawa, H., and Dowell, E. H., "An Elementary Explanation of the Flutter Mechanism with Active Feedback Controls," *Journal of Aircraft*, Vol. 16, No. 4, 1979, pp. 225–232. https://doi.org/10.2514/3.58509.

[5] Livne, E., "Aircraft Active Flutter Suppression: State of the Art and Technology Maturation Needs," *Journal of Aircraft*, Vol. 55, No. 1, 2018, pp. 410–452. https://doi.org/10.2514/1.c034442.

[6] Bisplinghoff, R. L., *Aeroelasticity*, Dover science books, Dover, New York, 1996. Edited by Holt Ashley and Robert L. Halfman.

[7] Tewari, A., *Aeroservoelasticity*, SpringerLink, Springer, New York, NY [u.a.], 2015.

[8] Nissim, E., "Flutter suppression using active controls based on the concept of aerodynamic energy," Tech. rep., NASA, 1971.

[9] Ballauf, C., "Dämpfung aeroelastischer Strukturenmit modelladaptiver Regelung," Ph.D. thesis, Technischen Universität München, 2007.

[10] Ohta, H., Fujimori, A., Nikiforuk, P. N., and Gupta, M. M., "Active flutter suppression for two-dimensional airfoils," *Journal of Guidance, Control, and Dynamics*, Vol. 12, No. 2, 1989, pp. 188–194. https://doi.org/10.2514/3.20390.

[11] Preumont, A., "Vibration Control of Active Structures: An Introduction," *Meccanica*, Vol. 34, No. 2, 1999, pp. 139–139. https://doi.org/10.1023/a:1004398914135.

[12] Wykes, J., "Structural dynamic stability augmentation and gust alleviation of flexible aircraft," *5th Annual Meeting and Technical Display*, American Institute of Aeronautics and Astronautics, 1968. https://doi.org/10.2514/6.1968-1067.

[13] Wykes, J. H., "Design and development of a structural mode control system," Tech. rep., NASA, 1977.

[14] Wykes, J. H., "Analyses and Tests of the B-1 Aircraft Structural Mode ControlSystem," Tech. rep., NASA, 1980.

[15] Roger, K. L., Hodges, G. E., and Felt, L., "Active Flutter Suppression-A Flight Test Demonstration," *Journal of Aircraft*, Vol. 12, No. 6, 1975, pp. 551–556. https://doi.org/10.2514/3.59833.

[16] Waszak, M. R., and Srinathkumar, S., "Flutter suppression for the active flexible wing - A classical design," *Journal of Aircraft*, Vol. 32, No. 1, 1995, pp. 61–67. https://doi.org/10.2514/3.46684.

[17] Schmidt, D., and Chen, T., "Frequency domain synthesis of a robust flutter suppression control law," *Journal of Guidance, Control, and Dynamics*, Vol. 9, No. 3, 1986, pp. 346–351. https://doi.org/10.2514/3.20112.

[18] Mukhopadhyay, V., "Flutter suppression control law design and testing for the active flexible wing," *Journal of Aircraft*, Vol. 32, No. 1, 1995, pp. 45–51. https://doi.org/10.2514/3.46682.

[19] Schmidt, D. K., "Stability Augmentation and Active Flutter Suppression of a Flexible Flying-Wing Drone," *Journal of Guidance, Control, and Dynamics*, Vol. 39, No. 3, 2016, pp. 409–422. https://doi.org/10.2514/1.g001484.

[20] Grauer, J. A., and Waite, J., "Design of a Collocation-Based Active Flutter Suppression Control Law for the IAWTM Wind Tunnel Model," *AIAA SCITECH 2024 Forum*, American Institute of Aeronautics and Astronautics, 2024. https://doi.org/10.2514/6.2024-2201.

[21] Mahesh, J., Stone, C., Garrard, W., and Dunns, H., "Control Law Synthesis for Flutter Suppression Using Linear Quadratic Gaussian Theory," *Journal of Guidance and Control*, Vol. 4, No. 4, 1981, pp. 415–422. https://doi.org/10.2514/3.56094.

[22] Newsom, J. R., Pototzky, A. S., and Abel, I., "Design of a flutter suppression system for an experimental drone aircraft," *Journal of Aircraft*, Vol. 22, No. 5, 1985, pp. 380–386. https://doi.org/10.2514/3.45135.

[23] Waszak, M. R., "Robust Multivariable Flutter Suppression for Benchmark Active Control Technology Wind-Tunnel Model," *Journal of Guidance, Control, and Dynamics*, Vol. 24, No. 1, 2001, pp. 147–153. https://doi.org/10.2514/2.4694.

[24] Zhao, Y., "Flutter suppression of a high aspect-ratio wing with multiple control surfaces," *Journal of Sound and Vibration*, Vol. 324, No. 3–5, 2009, pp. 490–513. https://doi.org/10.1016/j.jsv.2009.02.026.

[25] Huang, R., Hu, H., and Zhao, Y., "Designing active flutter suppression for high-dimensional aeroelastic systems involving a control delay," *Journal of Fluids and Structures*, Vol. 34, 2012, pp. 33–50. https://doi.org/10.1016/j.jfluidstructs.2012.05.012.

[26] Borglund, D., "The mu-k Method for Robust Flutter Solutions," *Journal of Aircraft*, Vol. 41, No. 5, 2004, pp. 1209–1216. https://doi.org/10.2514/1.3062.

[27] Theis, J., Pfifer, H., and Seiler, P. J., "Robust Control Design for Active Flutter Suppression," *AIAA Atmospheric Flight Mechanics Conference*, American Institute of Aeronautics and Astronautics, 2016. https://doi.org/10.2514/6.2016-1751.

[28] Svoboda, F., and Hromcik, M., "Active flutter suppression by means of fixed-order H Infinity control: results for the Benchmark Active Control Technology (BACT) wing," *2019 18th European Control Conference (ECC)*, IEEE, 2019, pp. 119–124. https://doi.org/10.23919/ecc.2019.8795733.

[29] Theis, J., "Robust and Linear Parameter-Varying Control of Aeroservoelastic Systems," Ph.D. thesis, Universität Hamburg, 2018.

[30] Hjartarson, A., Seiler, P. J., Packard, A., and Balas, G. J., "LPV Aeroservoelastic Control using the LPVTools Toolbox," *AIAA Atmospheric Flight Mechanics (AFM) Conference*, American Institute of Aeronautics and Astronautics, 2013. https://doi.org/10.2514/6.2013-4742.

[31] Barker, J. M., and Balas, G. J., "Comparing Linear Parameter-Varying Gain-Scheduled Control Techniques for Active Flutter Suppression," *Journal of Guidance, Control, and Dynamics*, Vol. 23, No. 5, 2000, pp. 948–955. https://doi.org/10.2514/2.4637.

[32] Barker, J. M., Balas, G. J., and Blue, P. A., "Gain-Scheduled Linear Fractional Control for Active Flutter Suppression," *Journal of Guidance, Control, and Dynamics*, Vol. 22, No. 4, 1999, pp. 507–512. https://doi.org/10.2514/2.4418.

[33] Danowsky, B. P., Thompson, P., Lee, D.-C., and Brenner, M. J., "Modal Isolation and Damping for Adaptive Aeroservoelastic Suppression," *AIAA Atmospheric Flight Mechanics (AFM) Conference*, American Institute of Aeronautics and Astronautics, 2013. https://doi.org/10.2514/6.2013-4743.

[34] Pusch, M., "Aeroelastic Mode Control using H2-optimal Blends for Inputs and Outputs," *2018 AIAA Guidance, Navigation, and Control Conference*, American Institute of Aeronautics and Astronautics, 2018. https://doi.org/10.2514/6.2018-0618.

[35] Pusch, M., Ossmann, D., and Luspay, T., "Structured Control Design for a Highly Flexible Flutter Demonstrator," *Aerospace*, Vol. 6, No. 3, 2019, p. 27. https://doi.org/10.3390/aerospace6030027.

[36] Pusch, M., and Ossmann, D., "$\mathcal{H}_2$ -Optimal Blending of Inputs and Outputs for Modal Control," *IEEE Transactions on Control Systems Technology*, Vol. 28, No. 6, 2020, pp. 2744–2751. https://doi.org/10.1109/tcst.2019.2942281.

[37] Skogestad, S., and Postlethwaite, I., *Multivariable feedback control*, 2nd ed., Wiley, Chichester, 2010.

[38] Litz, L., "Modale Maße für Steuerbarkeit, Beobachtbarkeit, Regelbarkeit und Dominanz - Zusammenhänge, Schwachstellen, neue Wege / Modal measures of Controllability, Observability, Dominance - Connections, Drawbacks and a new Approach," *auto*, Vol. 31, No. 1–12, 1983, pp. 148–158. https://doi.org/10.1524/auto.1983.31.112.148.

[39] Hamdan, A. M. A., and Nayfeh, A. H., "Measures of modal controllability and observability for first- and second-order linear systems," *Journal of Guidance, Control, and Dynamics*, Vol. 12, No. 3, 1989, pp. 421–428. https://doi.org/10.2514/3.20424.

[40] Hippe, P., "Ein modales Regelbarkeitsmaß für lineare, zeitinvariante dynamische Systeme / A measure for the influence of feedback control on the dynamics of linear, time-invariant systems," *auto*, Vol. 30, No. 1–12, 1982, pp. 96–101. https://doi.org/10.1524/auto.1982.30.112.96.

[41] Litz, L., "Berechnung stabilisierender Ausgangsvektorrückführungen über Polempfindlichkeiten / Stabilizing output-vector feedback via eigenvalue sensitivities," *auto*, Vol. 29, No. 1–12, 1981, pp. 434–440. https://doi.org/10.1524/auto.1981.29.112.434.

[42] Eichelsdörfer, J., "Open-Source Benchmark Model for Active Flutter Suppression," *submitted for AIAA Scitech 2026 Forum*, 2026.

[43] Albano, E., and Rodden, W., "A doublet-lattice method for calculating lift distributions on oscillating surfaces in subsonic flows." *AIAA Journal*, Vol. 7, No. 2, 1969, pp. 279–285. https://doi.org/10.2514/3.5086.

[44] Blair, M., "A Compilation of the Mathematics Leading to the Doublet Lattice Method," Tech. rep., Air Force Wright Laboratory, 1992.

[45] Böhnisch, N., Braun, C., Koschel, S., and Marzocca, P., "Whirl Flutter for Distributed Propulsion Systems on a Flexible Wing," *AIAA SCITECH 2022 Forum*, American Institute of Aeronautics and Astronautics, 2022. https://doi.org/10.2514/6.2022-1755.

[46] Roger, "Structural Aspects of Active Controls." *Agard Conference Proceedings*, 1977.

[47] Karpel, M., "Design for Active Flutter Suppression and Gust Alleviation Using State-Space Aeroelastic Modeling," *Journal of Aircraft*, Vol. 19, No. 3, 1982, pp. 221–227. https://doi.org/10.2514/3.57379.

[48] Kier, T., and Looye, G., "Unifying Manoeuvre and Gust Loads Analysis Models," *International Forum on Aeroelasticity and Structural Dynamics (IFASD)*, 2009.

[49] Stalla, F., Kier, T. M., Looye, G., and Pusch, M., "Aeroservoelastic Modeling and Robust Control for Gust Load Alleviation of an Experimental Wing," *AIAA SCITECH 2024 Forum*, American Institute of Aeronautics and Astronautics, 2024. https://doi.org/10.2514/6.2024-1442.

[50] Theis, J., Pfifer, H., and Seiler, P., "Robust Modal Damping Control for Active Flutter Suppression," *Journal of Guidance, Control, and Dynamics*, Vol. 43, No. 6, 2020, pp. 1056–1068. https://doi.org/10.2514/1.g004846.

[51] Apkarian, P., and Noll, D., "Nonsmooth H Infinity Synthesis," *IEEE Transactions on Automatic Control*, Vol. 51, No. 1, 2006, pp. 71–86. https://doi.org/10.1109/tac.2005.860290.

[52] Apkarian, P., Gahinet, P., and Buhr, C., "Multi-model, multi-objective tuning of fixed-structure controllers," *2014 European Control Conference (ECC)*, IEEE, 2014. https://doi.org/10.1109/ecc.2014.6862200.

[53] Seiler, P., Packard, A., and Gahinet, P., "An Introduction to Disk Margins [Lecture Notes]," *IEEE Control Systems*, Vol. 40, No. 5, 2020, pp. 78–95. https://doi.org/10.1109/mcs.2020.3005277.

[54] Stein, G., "Respect the Unstable," *IEEE Control Systems*, Vol. 23, No. 4, 2003, pp. 12–25. https://doi.org/10.1109/mcs.2003.1213600.